Biophysical Reports

REPORT

Establishing Riboglow-FLIM to visualize noncoding RNAs inside live zebrafish embryos

Nadia Sarfraz,[1] Harrison J. Lee,[1] Morgan K. Rice,[1] Emilia Moscoso,[1] Luke K. Shafik,[1] Eric Glasgow,[2] Suman Ranjit,[3,4] Ben J. Lambeck,[1] and Esther Braselmann[1,*]

[1]Department of Chemistry, Georgetown University, Washington, District of Columbia; [2]Department of Oncology, Lombardi Comprehensive Cancer Center, Georgetown University Medical Center, Washington, District of Columbia; [3]Department of Biochemistry and Molecular & Cellular Biology, Georgetown University, Washington, District of Columbia; and [4]Microscopy & Imaging Shared Resource, Georgetown University, Washington, District of Columbia

ABSTRACT The central role of RNAs in health and disease calls for robust tools to visualize RNAs in living systems through fluorescence microscopy. Live zebrafish embryos are a popular system to investigate multicellular complexity as disease models. However, RNA visualization approaches in whole organisms are notably underdeveloped. Here, we establish our RNA tagging and imaging platform Riboglow-FLIM for complex cellular imaging applications by systematically evaluating FLIM capabilities. We use adherent mammalian cells as models for RNA visualization. Additional complexity of analyzing RNAs in whole mammalian animals is achieved by injecting these cells into a zebrafish embryo system for cell-by-cell analysis in this model of multicellularity. We first evaluate all variable elements of Riboglow-FLIM quantitatively before assessing optimal use in whole animals. In this way, we demonstrate that a model noncoding RNA can be detected robustly and quantitatively inside live zebrafish embryos using a far-red Cy5-based variant of the Riboglow platform. We can clearly resolve cell-to-cell heterogeneity of different RNA populations by this methodology, promising applicability in diverse fields.

WHY IT MATTERS The discovery of fluorescent proteins and subsequent engineering efforts have revolutionized fields across biology, but comparable tools to visualize RNAs live are critically lacking. Here, we demonstrate that our RNA Riboglow-FLIM platform may fill this need. Of note, we establish that Riboglow-FLIM requires fluorescence lifetime imaging microscopy (FLIM). The fluorophore element in Riboglow-FLIM is variable, hence a far-red fluorophore for use in live multicellular environments can be used after careful biophysical characterization. We make use of the common strategy to inject mammalian cells producing a fluorescence sensor into live embryos as a systematic step of introducing complexity of a multicellular environment. Here, we demonstrate that different cellular conditions produce heterogeneous Riboglow-FLIM signatures that can be quantitatively differentiated.

Zebrafish embryos are a common model organism for studying aspects of human diseases with cell-by-cell resolution (1), as they enable insights into multicellular processes in the context of whole organisms with relative ease (2). The similarity between zebrafish and human genomes, and their similar organ systems and cellular functions make zebrafish embryos a particularly valuable model for cancer cell metastasis investigations (1,3,4). The embryo's optical transparency inspired adaptation of imaging techniques for studying complex cell biology live (1). Importantly, zebrafish embryos are a common model to establish multicellular imaging systems by injecting mammalian cells expressing well-characterized sensors in the embryo (5,6). This allows for assessing complex fluorescence imaging in a multicellular environment systematically (7). RNAs play critical roles in many biological processes, and investigating them in living organisms is essential for insights in health and disease. While great progress has been made in designing fluorescence RNA sensors, approaches for visualizing RNAs in multicellular environments or whole organisms are lacking (8–16), with the notable exception of the MS2 technology applications (17). Investigating RNAs in multicellular environments is particularly relevant in cancer biology, where RNA

Submitted June 13, 2023, and accepted for publication September 21, 2023.

*Correspondence: esther.braselmann@georgetown.edu

Editor: Ulrike Endesfelder.

https://doi.org/10.1016/j.bpr.2023.100132

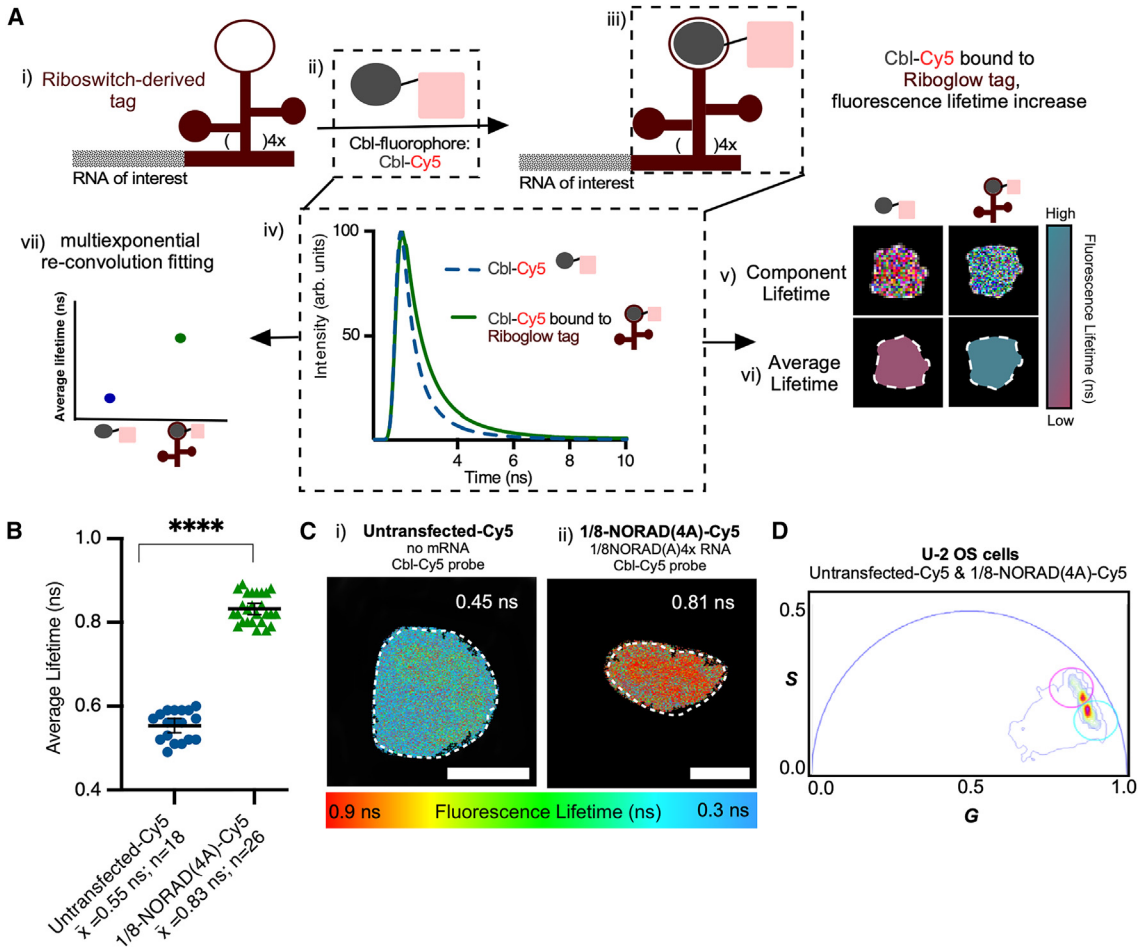

FIGURE 1 Visualizing RNAs live with Riboglow-FLIM-Cy5. (*A*) Cobalamin (Cbl) is synthetically linked to Cy5, quenches its fluorescence, binds an RNA ligand (called the "A-tag" throughout), and alters its fluorescence lifetime. The RNA tag is genetically fused to an RNA of interest. Fluorescence lifetime decay data are fit by multiexponential reconvolution for a defined region of interest (ROI), yielding component and average lifetime (both are amplitude-weighted lifetimes, see methods for details). Both can be illustrated by a false-color scale. The "component lifetime" (v) resolves the lifetime pixel-by-pixel, while the "average lifetime" (vi, vii) provides one lifetime value per ROI. (*B*) Riboglow-FLIM-Cy5 in live cells (4 independent experiments, 44 cells, 1 symbol = 1 cell). One-way ANOVA (95% confidence limit); post hoc test (Tukey HSD), p-value listed (****p $\leq$ 0.0001). Error bars: mean and standard deviation ($\pm$SD). (*C*) Representative cells from (*B*), component lifetimes displayed. Scale bars, 10 μm. (*D*) Phasor plot showing graphical representation of lifetime coordinates *G* and *S* for all data shown in (*B*). Light blue circle, untransfected cells; pink circle, transfected cells producing 1/8-NORAD(4A), 4 independent experiments, 44 cells. Phasor representative images shown in Fig. S2 D.

processes are often misregulated (18). We recently developed Riboglow-FLIM for visualizing RNAs live and quantitatively with subcellular precision using FLIM (19). Riboglow-FLIM consists of an RNA tag that is genetically fused to an RNA of interest and binds a fluorescent small-molecule ligand tightly (Fig. 1 *A*) (16). The FLIM readout modality enables concentration-independent RNA imaging live, making this platform an ideal system to evaluate applicability quantitatively in diverse and complex systems (19).

To evaluate Riboglow-FLIM's applicability in a multicellular model, we characterized the photophysical features of the platform by systematically introducing complexity one element at a time (Fig. S1 *A*). We reasoned that the far-red Cbl-Cy5 variant of Riboglow-FLIM (Riboglow-FLIM-Cy5) would achieve imaging depth (16,20). Cy5 is frequently used in live cells or organisms due to its biocompatibility (21,22), brightness, and high photostability, coupled with minimal light absorption and scattering in tissues (20–22). Here, we demonstrate that Riboglow-FLIM-Cy5 (16,19) enables quantitative detection of RNAs in cells in the context of live zebrafish embryos. We envision that Riboglow-FLIM-Cy5 will lead to advancing our understanding of RNA behavior in multicellular environments in diverse disease applications.

We began by adapting the Riboglow-FLIM platform to far-red fluorescence to minimize tissue autofluorescence in the complex multicellular environment (20).

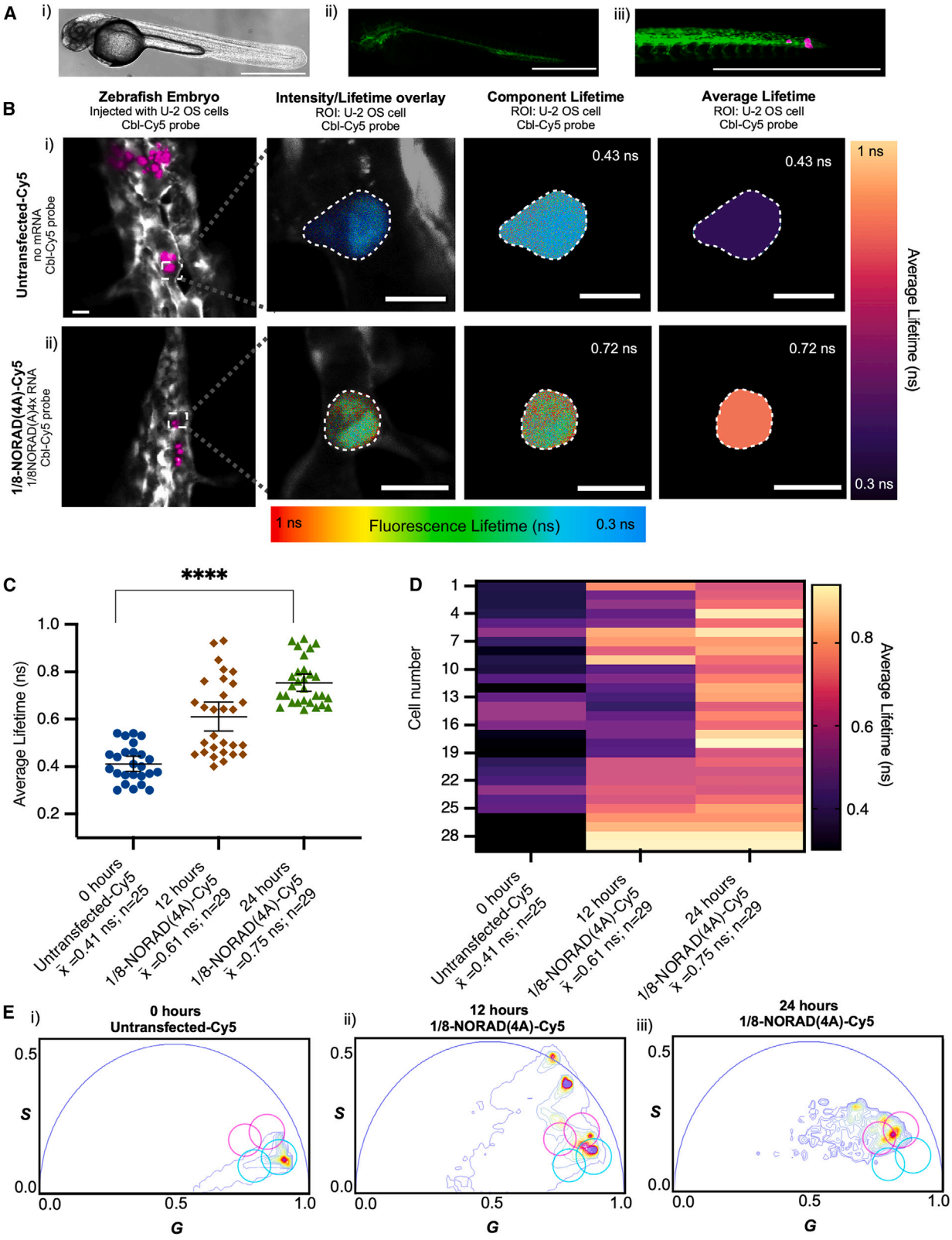

FIGURE 2 Quantitative assessment of Riboglow-FLIM-Cy5 in live zebrafish embryos. (*A*) Live transgenic zebrafish embryos producing GFP in embryo vasculature were injected with live U-2 OS cells. (i) Bright-field image: (ii and iii) fluorescence images: green, GFP (vascular); purple, Cy5 from Cbl-Cy5. Cells either remained (i) untransfected or were (ii) previously transfected with a plasmid producing 1/8-NORAD(4A) RNA and loaded with Cbl-Cy5. Scale bars, 750 μm. (*B*) Representative cells that were injected into zebrafish embryos are shown. Untransfected (*top*) and

For this, we chose the Cbl-Cy5 probe (13). We first asked if fluorescence lifetime changes of the Cbl-Cy5 probe were robust in the presence and absence of our established Riboglow RNA tag ("A-tag" (19) throughout, Fig. 1 *A*). Our hypothesis to expand Riboglow-FLIM with the Cbl-Cy5 probe is based on the previous observation that the Cbl-4xGly-ATTO 590 probe yields strong contrast in fluorescence lifetime experiments in the presence of the RNA tag (19). Furthermore, Cbl-Cy5 results in fluorescence intensity changes upon RNA ligand binding, suggesting that it might be compatible with Riboglow-FLIM also (16,19). We analyzed the fluorescence intensity values (Fig. S2 *B*) in comparison with commonly used FLIM data analyses, namely analyzing amplitude-weighted and intensity-weighted fluorescence lifetime (see methods for details, and Fig. S1, note that we refer to amplitude-weighted lifetime as "fluorescence lifetime" throughout this work). We fit lifetime data by multiexponential reconvolution per region of interest (ROI) (19) for samples of Cbl-Cy5 with and without the purified RNA A-tag. FLIM data fitting was assessed by evaluating residual maps of fluorescence decays (see methods for details). As expected, we observed a significant increase in fluorescence lifetime for Cbl-Cy5 in the presence of purified RNA (Fig. S2, *A* and *B* ii). This is in line with the rationale that the Cbl probe moiety binds the RNA and that this interaction affects the fluorescence properties of Cy5.

We next predicted that combining Riboglow-FLIM with the Cbl-Cy5 probe will allow visualization of RNAs in live adherent mammalian cells reliably with the ultimate goal to assess performance in complex multicellular environments. We chose a truncation of the long noncoding RNA NORAD (23) fused with four copies of our A-tag as the model RNA (19) (abbreviated as 1/8-NORAD(4A) here) for imaging live U-2 OS cells, as we have employed this RNA model previously (19). A plasmid producing 1/8-NORAD(4A) was transiently transfected in U-2 OS cells, the Cbl-Cy5 probe was loaded into the cell, and live cell FLIM images were collected. For analysis, single whole cells were defined as ROIs and the lifetime was extracted by multiexponential reconvolution as established with the in vitro system above (Fig. 1 *C* i vs. ii and Fig. S1, *A* and *B*). As for the purified RNA system, we systematically compared multiexponential reconvolution (amplitude-weighted and intensity-weighted lifetimes) in comparison with the fluorescence intensity readout for live cells (Figs. 1 *C* and S2 *C*). As an additional analysis method of FLIM, we used the common fit-free phasor approach (Figs. 1 *D*, S1 *D*, and S2 *D*). We note that multiexponential reconvolution makes assumptions about goodness of fit and number of photons required for robust fitting (see methods for details), while the phasor approach is fit-free and hence an entirely orthogonal analysis approach (24–26). While we do observe clear differences in fluorescence signal when analyzing the fluorescence intensity (16,19), FLIM analysis consistently yields stronger contrast (Figs. 1 *B*, 2 *C*, and S2 *C*). As expected, Riboglow-FLIM-Cy5 is sensitive to visualize 1/8-NORAD(4A) with strong cellular contrast regardless of FLIM data analysis method (Figs. 1, *B–D*, S1, and S2, *C* and *D*).

The successful live cell measurements led us to predict that we could use Riboglow-FLIM-Cy5 to robustly visualize tagged RNAs in zebrafish embryos, expanding the complexity of the Riboglow platform (Fig. S1 A). We evaluated production of our model RNA in U-2 OS adherent cells throughout a relevant time course (Fig. S3) after fixation. We assessed production of our Riboglow-tagged model RNA by fluorescence *in situ* hybridization (FISH) using a probe that targets the Riboglow A-tag (Fig. S3). As observed previously (19), U-2 OS cells readily produce this Riboglow-tagged RNA, detectable by FISH. When comparing cell populations before transfection of the reporter and 12 vs. 24 h after transfection, we observed several trends (Fig. S3). First, Riboglow-tagged RNA was not detectable before transfection, as expected. Second, RNA accumulation was apparent 24 h post-transfection throughout the cell, with lower levels at 12 h, indicating production of RNA over time. Third, we observed that cells accumulate RNAs in speckles-resembling features, in particular at 12 h post-transfection. This observation is

transfected (*bottom*), both loaded with Cbl-Cy5. The fluorescence lifetime image overlaid with the intensity image shows zebrafish physiology in gray (from the GFP signal of transgenic embryos). The "component lifetime" illustrates fluorescence lifetime pixel-by-pixel, rainbow color scale. The "average lifetime" is illustrated by a heatmap color scale. (*C*) Average lifetimes of 1/8-NORAD(4A) tagged with Riboglow-FLIM-Cy5, injected into zebrafish embryos. Fluorescence lifetime was measured at 0, 12, and 24 h post-transfection. One dot = one whole cell in the context of a zebrafish embryo. Average fluorescence lifetime for 12 independent experiments, 83 cells; 1 symbol = 1 cell. One-way ANOVA (95% confidence limit); post hoc test (Tukey HSD), p value listed (****p $\leq$ 0.0001). Error bars = mean and standard deviation ($\pm$SD). Scale bar, 10 μm. (*D*) Heatmap representation of data in (*C*) where each average lifetime data point was assigned to a color in the heatmap. (*E*) Phasor plot showing graphical representation of lifetime coordinates *G* and *S* for all the data shown in (*C*). Light blue circle, reference for untransfected cells; pink circle, reference for transfected cells producing 1/8-NORAD(4A), 12 independent experiments, 83 cells. Phasor representative images shown in Fig. S4 B. Note that, at the 12 h time point, the GFP lifetime readout from the GFP produced in zebrafish embryo vasculature used as an internal control (see methods) was present. The lifetime from GFP creates two secondary phasor distributions on longer lifetimes and appear at longer phase angles.

perhaps indicative of often-described NORAD-containing granules (23). Finally, we note that a shift from no RNA expression to a majority of speckles to overproduction of model RNA throughout the cell is dependent on time post-transfection, in line with RNA production over time (Fig. S3). While subcellular RNA localization patterns are of interest for future investigations, we decided to focus on overall cell-by-cell RNA levels here. We estimated overall RNA levels per cell by quantifying the FISH signal per cell for all experimental conditions (Fig. S3 *C*) and found an increase in signal and a broad distribution of cellular RNA levels, represented by large error bars (Fig. S3 *C*). The observed heterogeneity in reporter RNA levels led us to ask whether such heterogeneous patterns can be resolved in the multicellular environment with the Riboglow-FLIM platform.

We evaluated cell-by-cell heterogeneity of our model RNA phenotypes by FLIM in zebrafish next. For this, U-2 OS cells producing our model RNA, 1/8-NORAD(4A), were injected into live sedated zebrafish embryos that constitutively produce vascular GFP (Fig. 2 *A*) (27). As for adherent cells, samples were imaged by FLIM, ROIs of individual cells within the zebrafish were defined (Fig. 2 *B*), and lifetime values were extracted (Fig. S1). Importantly, trends of a cell-by-cell analysis in the context of zebrafish matched observations obtained at the single-cell level (compare Figs. 1, *B* and *C* and 2 *B*).

We hypothesized that Riboglow-FLIM-Cy5 could quantitatively describe more subtle cell-by-cell variabilities in the complex zebrafish embryo environment. For this, we used the previously observed heterogeneity in the single-cell FISH system as a basis, where we evaluated the RNA reporter at 0, 12, and 24 h post-transfection in U-2 OS cells (Fig. S3). We transfected U-2 OS cells with 1/8-NORAD(4A) and injected cells into zebrafish embryos at 0, 12, and 24 h post-transfection, covering a time frame where production of the transiently transfected model RNA would increase, and cells would exhibit well-characterized 1/8-NORAD(4A) heterogeneity (Fig. S3). The clearly detectable trend of increasing 1/8-NORAD(4A) by FISH at these time points (Fig. S3) serves as the foundation here, indicating a steady accumulation of cellular reporter RNA throughout this time window. We expected to capture a steady increase in the Riboglow-FLIM-Cy5 readout in the zebrafish system, mirroring a shift from the untransfected population to the transfected population (Fig. 2 *B*). Indeed, the 0 and 24 h cells exhibited two differentiable lifetime values, where the 0 h cells exhibited lifetimes similar to that of the unbound (Cbl-Cy5) probe as in untransfected cells. Conversely, the 24 h cells were similar to cells after reporter RNA overexpression (Fig. 2 *B* vs. Fig. 1, *B* and *D*, vs. Fig. 2 *E*). We hypothesized that 12 h post-transfection cells would result in intermediate levels of RNAs per cell with some unbound probe, resulting in a homogeneous average fluorescence lifetime between the two ends. Surprisingly, though, we observed two distinct FLIM populations at 12 h post-transfection (Figs. 2 *C* and S4 *A*). Importantly, the cells used for injecting embryos originated from the same transfected cell population and the lifetime heterogeneity was observed independent of embryo sample, timing of imaging, or location within the embryo. Remarkably, two representative neighboring cells in the same embryo exhibited the two distinct lifetime values (Fig. S4, *A* and *B*). Upon closer comparison, we determined that these two populations resembled the lifetime readouts of the 0 and 24 h cell populations (Fig. 2 *B*). To confirm this, we pooled the 0 and 24 h readouts, compared them directly to the 12 h batch and observed no significant difference (Fig. S4 *C*). Together, we find that Riboglow-FLIM-Cy5 enables robust visualization of RNAs in the context of live zebrafish embryos and we can quantitatively assess live cellular populations. Similar to FISH, we resolved distinct RNA populations over time. We hypothesize that this heterogeneity may arise from differences in RNA transcription rates or post-transcriptional modifications within specific cellular subpopulations. Further investigations are needed to elucidate the underlying mechanisms driving this dual RNA population phenomenon and its functional implications. We anticipate that Riboglow-FLIM-Cy5 can be used to describe and track RNAs in this and other multicellular systems quantitatively to investigate RNA processes. Another possible next application may be expansion of deep-tissue FLIM imaging with Cy5 by two-photon microscopy in whole organs and/or animals.

DATA AND CODE AVAILABILITY

The data used in this publication can be accessed in a separate repository: https://dx.doi.org/10.6084/m9.figshare.24103086.

SUPPORTING MATERIAL

Supplemental information can be found online at https://doi.org/10.1016/j.bpr.2023.100132.

AUTHOR CONTRIBUTIONS

E.B. conceived the study. N.S. conceived and performed the analysis. N.S., H.J.L., and E.M. collected data and performed analysis. B.J.L. performed FISH image analysis. M.K.R., E.M., and L.K.S. assisted in data collection. E.G. prepared zebrafish embryo samples. S.R. performed phasor analysis. N.S. wrote the manuscript with edits and comments from all authors.

ACKNOWLEDGMENTS

The authors would like to thank R. Maillard for helpful discussions. They would also like to acknowledge financial support from the NIH (R00GM127752 and R35GM150823 to E.B.), the Luce Foundation (to E.B. and M.K.R.), Georgetown College, the Georgetown Chemistry Department (Espenscheid Fellowship to L.K.S.), the DAAD RISE program (to B.J.L.), and the American Cancer Society (ACS IRG 17-177-23, pilot award to E.B., PI: Riggins). This research was supported by the Animal Models Shared Resource and Microscopy & Imaging Shared Resource Center of the Georgetown Lombardi Comprehensive Cancer Center (P30-CA051008) and Tissue Culture and Biobanking Shared Resource (Georgetown University).

DECLARATION OF INTERESTS

The authors declare no competing interests.

REFERENCES

1. White, R., K. Rose, and L. Zon. 2013. Zebrafish cancer: the state of the art and the path forward. *Nat. Rev. Cancer.* 13:624–636.
2. Xiao, J., E. Glasgow, and S. Agarwal. 2020. Zebrafish Xenografts for Drug Discovery and Personalized Medicine. *Trends Cancer.* 6:569–579.
3. Dooley, K., and L. I. Zon. 2000. Zebrafish: a model system for the study of human disease. *Curr. Opin. Genet. Dev.* 10:252–256.
4. Sacco, A., A. M. Roccaro, …, I. M. Ghobrial. 2016. Cancer Cell Dissemination and Homing to the Bone Marrow in a Zebrafish Model. *Cancer Res.* 76:463–471.
5. Teng, Y., X. Xie, …, J. K. Cowell. 2013. Evaluating human cancer cell metastasis in zebrafish. *BMC Cancer.* 13:453.
6. Rouhi, P., L. D. Jensen, …, Y. Cao. 2010. Hypoxia-induced metastasis model in embryonic zebrafish. *Nat. Protoc.* 5:1911–1918.
7. Qin, X., F. F. J. Laroche, …, H. Feng. 2020. In Vivo Targeting of Xenografted Human Cancer Cells with Functionalized Fluorescent Silica Nanoparticles in Zebrafish. *JoVE*e61187. https://doi.org/10.3791/61187.
8. Sunbul, M., J. Lackner, …, A. Jäschke. 2021. Super-resolution RNA imaging using a rhodamine-binding aptamer with fast exchange kinetics. *Nat. Biotechnol.* 39:686–690.
9. Paige, J. S., K. Y. Wu, and S. R. Jaffrey. 2011. RNA mimics of green fluorescent protein. *Science.* 333:642–646.
10. Filonov, G. S., J. D. Moon, S. R. Jaffrey…, 2014. Broccoli: rapid selection of an RNA mimic of green fluorescent protein by fluorescence-based selection and directed evolution. *J. Am. Chem. Soc.* 136:16299–16308.
11. Bertrand, E., P. Chartrand, …, R. M. Long. 1998. Localization of ASH1 mRNA particles in living yeast. *Mol. Cell.* 2:437–445.
12. Dolgosheina, E. V., S. C. Y. Jeng, …, P. J. Unrau. 2014. RNA mango aptamer-fluorophore: a bright, high-affinity complex for RNA labeling and tracking. *ACS Chem. Biol.* 9:2412–2420.
13. Chen, X., D. Zhang, …, Y. Yang. 2019. Visualizing RNA dynamics in live cells with bright and stable fluorescent RNAs. *Nat. Biotechnol.* 37:1287–1293.
14. Bouhedda, F., K. T. Fam, …, M. Ryckelynck. 2020. A dimerization-based fluorogenic dye-aptamer module for RNA imaging in live cells. *Nat. Chem. Biol.* 16:69–76.
15. Arora, A., M. Sunbul, and A. Jäschke. 2015. Dual-colour imaging of RNAs using quencher- and fluorophore-binding aptamers. *Nucleic Acids Res.* 43:e144.
16. Braselmann, E., A. J. Wierzba, …, A. E. Palmer. 2018. A multicolor riboswitch-based platform for imaging of RNA in live mammalian cells. *Nat. Chem. Biol.* 14:964–971.
17. Lionnet, T., K. Czaplinski, …, R. H. Singer. 2011. A transgenic mouse for in vivo detection of endogenous labeled mRNA. *Nat. Methods.* 8:165–170.
18. Prensner, J. R., and A. M. Chinnaiyan. 2011. The emergence of lncRNAs in cancer biology. *Cancer Discov.* 1:391–407.
19. Sarfraz, N., E. Moscoso, …, E. Braselmann. 2023. Visualizing orthogonal RNAs simultaneously in live mammalian cells by fluorescence lifetime imaging microscopy (FLIM). *Nat. Commun.* 14:867.
20. Adjili, S., A. Favier, …, M. T. Charreyre. 2015. Biocompatible photoresistant far-red emitting, fluorescent polymer probes, with near-infrared two-photon absorption, for living cell and zebrafish embryo imaging. *Biomaterials.* 46:70–81.
21. Shcherbo, D., E. M. Merzlyak, …, D. M. Chudakov. 2007. Bright far-red fluorescent protein for whole-body imaging. *Nat. Methods.* 4:741–746.
22. Hilderbrand, S. A., and R. Weissleder. 2010. Near-infrared fluorescence: application to in vivo molecular imaging. *Curr. Opin. Chem. Biol.* 14:71–79.
23. Matheny, T., B. Van Treeck, …, R. Parker. 2021. RNA partitioning into stress granules is based on the summation of multiple interactions. *RNA.* 27:174–189.
24. Ranjit, S., L. Malacrida, …, E. Gratton. 2018. Fit-free analysis of fluorescence lifetime imaging data using the phasor approach. *Nat. Protoc.* 13:1979–2004.
25. Digman, M. A., V. R. Caiolfa, …, E. Gratton. 2008. *Biophys. J.* 94:L14–L16.
26. Malacrida, L., S. Ranjit, …, E. Gratton. 2021. The Phasor Plot: A Universal Circle to Advance Fluorescence Lifetime Analysis and Interpretation. *Annu. Rev. Biophys.* 50:575–593.
27. Roth, S. M., E. B. Berens, …, A. Wellstein. 2021. Cancer Cell Invasion and Metastasis in Zebrafish Models (Danio rerio). *Methods Mol. Biol.* 2294:3–16. https://doi.org/10.1007/978-1-0716-1350-4_1.